Title: Aberrant activation of wound healing programs within the metastatic niche facilitates lung colonization by osteosarcoma cells

Author list: James B. Reinecke[1,2], Amy C. Gross[1], Maren Cam[1], Leyre Jimenez Garcia[3], Matthew V. Cannon[1], Ruben Dries[4,5], Berkley E. Gryder[6], Ryan D. Roberts[1,2,7]

Author affiliations:

[1] Center for Childhood Cancer Research, Abigail Wexner Research Institute, Nationwide Children's Hospital, Columbus, OH

[2] Department of Hematology, Oncology, and Bone Marrow Transplant, Nationwide Children's Hospital, Columbus, OH

[3] Molecular, Cellular, and Developmental Biology Program, The Ohio State University, Columbus, OH

[4] Section of Hematology and Medical Oncology, Boston University School of Medicine and Boston Medical Center, Boston, MA

[5] Division of Computational Biomedicine, Boston University School of Medicine, Boston, MA

[6] Department of Genetics and Genome Sciences, Case Western Reserve University School of Medicine, Cleveland, OH

[7] The Ohio State University James Comprehensive Cancer Center, Columbus, OH

Running title: Abnormal wound healing promotes osteosarcoma metastasis

Corresponding author contact: Ryan Roberts, ryan.roberts@nationwidechildrens.org

Abstract

Purpose:

Lung metastasis is responsible for nearly all deaths caused by osteosarcoma, the most common pediatric bone tumor. How malignant bone cells coerce the lung microenvironment to support metastatic growth is unclear. This study delineates how osteosarcoma cells educate the lung microenvironment during metastatic progression.

Experimental design:

Using single-cell transcriptomics (scRNA-seq), we characterized genome- and tissue-wide molecular changes induced within lung tissues by disseminated osteosarcoma cells in both immunocompetent murine models of metastasis and patient samples. We confirmed transcriptomic findings at the protein level and determined spatial relationships with multi-parameter immunofluorescence. We evaluated the ability of nintedanib to impair metastatic colonization and prevent osteosarcoma-induced education of the lung microenvironment in both immunocompetent murine osteosarcoma and immunodeficient human xenograft models.

Results:

Osteosarcoma cells induced acute alveolar epithelial injury upon lung dissemination. scRNA-seq demonstrated that the surrounding lung stroma adopts a chronic, non-resolving wound-healing phenotype similar to that seen in other models of lung injury. Accordingly, metastasis-associated lung demonstrated marked fibrosis, likely due to the accumulation of pathogenic, pro-fibrotic, partially-differentiated epithelial intermediates. Inhibition of fibrotic pathways with nintedanib prevented metastatic progression in multiple murine and human xenograft models.

Conclusions:

Our work demonstrates that osteosarcoma cells co-opt fibrosis to promote metastatic outgrowth. When harmonized with data from adult epithelial cancers, our results support a generalized model wherein aberrant mesenchymal-epithelial interactions are critical for promoting lung metastasis. Adult epithelial carcinomas induce fibrotic pathways in normal lung fibroblasts, whereas osteosarcoma, a pediatric mesenchymal tumor, exhibits fibrotic reprogramming in response to the aberrant wound-healing behaviors of an otherwise normal lung epithelium, which are induced by tumor cell interactions.

Statement of translational relevance:

Therapies that block metastasis have the potential to save the majority of lives lost due to solid tumors. Disseminated tumor cells must educate the foreign, inhospitable microenvironments they encounter within secondary organs to facilitate metastatic colonization. Our study elucidated that disseminated osteosarcoma cells survive within the lung by co-opting and amplifying the lung's endogenous wound healing response program. More broadly, our results support a model wherein mesenchymal-epithelial cooperation is a key driver of lung metastasis. Osteosarcoma, a pediatric mesenchymal tumor, undergoes lung epithelial induced fibrotic activation while also transforming normal lung epithelial cells towards a fibrosis promoting phenotype. Conversely, adult epithelial carcinomas activate fibrotic signaling in normal lung mesenchymal fibroblasts. Our data implicates fibrosis and abnormal wound healing as key drivers of lung metastasis across multiple tumor types that can be targeted therapeutically to disrupt metastasis progression.

Introduction

Metastasis is responsible for nearly all solid tumor-related deaths [1]. Metastasis proceeds through a multistep process wherein tumor cells invade the surrounding normal tissue adjacent to the primary tumor, enter the blood stream (for tumors that spread via hematogenous route), colonize, and ultimately grow within a distant tissue [2]. Preclinical and patient-level data suggest that therapies designed to disrupt the early steps of the metastatic cascade, such as invasion through adjacent tissues and intravasation into the bloodstream, are less likely to prevent clinically-relevant metastatic lesions, as disseminated malignant cells have likely colonized distant tissues prior to the detection of a primary tumor [3-5]. Development of therapies that target the later elements of the metastatic cascade are more likely to have clinical impact but have remained largely theoretical due to a crude understanding of the mechanisms that drive the colonization of distant tissues. Understanding how disseminated tumor cells transform the foreign and otherwise hostile microenvironments of metastatic sites into accommodating environments that promote tumor growth may expose novel metastatic vulnerabilities [6].

The lung is a common site of metastasis for tumors that originate in diverse developmental origins [7]. Physiologically, the lung not only facilitates gas exchange, but also creates a barrier to the invasion of microbes, toxins, pollutants, and allergens. Accordingly, the lung has evolved complex mechanisms for recognizing and repairing injury without causing excessive tissue damage or inflammation [8]. Certain pathological conditions such as idiopathic pulmonary fibrosis (IPF) arise when the mechanisms of lung repair become altered. In these altered states, dysregulation of these wound healing mechanisms leads to progressive dysfunction [9]. At the cellular level, IPF is

characterized by epithelial hyperplasia, accumulation of fibroblasts, and the excessive deposition of extracellular matrix (ECM) proteins such as fibronectin and collagen, all confined within an immunosuppressive microenvironment [10]. How these structural elements of the lung respond to metastatic cancer cells remains poorly understood. The profoundly inefficient nature of the metastatic process and the dramatic differences evident in the comparison of normal lung to metastatic lesions suggest that the soil of the lung must be shaped by cancer cells in order for tumors to successfully colonize and grow in the organ [11]. Therefore, disrupting the tumor education of the lung microenvironment is an attractive therapeutic approach to targeting metastatic disease.

Osteosarcoma is the most common malignant bone tumor in young people and ostensibly metastasizes to the lung, leading to poor patient outcomes [12-14]. Given the organotropism that osteosarcoma displays for the lung, and the critical clinical problem lung metastasis poses to patients with osteosarcoma, we leveraged several murine and human xenograft models to elucidate how the lung responds to metastatic osteosarcoma cells. We uncovered that osteosarcoma cells arrest within the distal alveolar epithelial niche, damage alveolar epithelial cells, and trigger an abnormal alveolar wound healing program that promotes metastatic progression. Utilizing single cell-RNA sequencing (scRNA-seq), we found that the stroma of established metastases resembles a fibrotic, non-healing wound. Translationally, disrupting the lung fibrosis response with nintedanib, a tyrosine kinase inhibitor (TKI) utilized clinically for treating patients with IPF, slowed osteosarcoma metastasis by reprogramming the metastatic microenvironment. Collectively, our study sheds light on how tumors co-opt the lung microenvironment during

metastasis and provides proof-of-concept that targeting the metastatic niche is a viable therapeutic strategy.

Materials and methods

Cell culture

All cell lines utilized herein were routinely authenticated with STR and mycoplasma testing through Laboratory Corporation of America. Cells utilized for experiments were within 20 passage doublings after reviving from liquid nitrogen storage. OS-17 cells were derived from an early passage of the OS-17 patient-derived xenograft created from a primary femur biopsy performed at St. Jude's Children's Research Hospital in Memphis and was a gift from Peter Houghton. OS-25 cells were a gift from Øystein Fodstad's lab at the Radium Hospital in Oslo [15]. K7M2 cells are a highly metastatic derivative cell line derived from a spontaneous osteosarcoma in a BALB/c mouse and were obtained from the American Type Culture Collection (ATCC, CRL2836). F420 cells are a murine osteosarcoma derived from spontaneous lung metastases arising in the genetically engineered osteosarcoma mouse model Col2a-Cre mutant Tp53 and was a gift from Jason Yustine. HBEC3-KT (HBEC) are an immortalized non-tumorigenic human lung epithelial cell line and were obtained from the ATCC (CRL-4051). F420 and K7M2 cells were propagated in culture in DMEM (Corning, 10-013-CV) supplemented with 10% fetal bovine serum (FBS) (R&D Systems, S11150H) while OS-17 cells were cultured in RPMI (Corning, 10-040-CV) supplemented with 10% FBS. HBEC cells were propagated in human airway epithelial media (ATCC, PCS-300-030) with the Bronchial Epithelial Cell Growth Kit (ATCC, PCS-300-040). OS-17 and HBEC cells were plated 1:1 on to glass coverslips in DMEM/F12 (Corning, 10-092-CV**)** supplemented with 1% FBS. HBEC

conditioned media was obtained after 72 hours of incubation (DMEM/F12 with 1% FBS) and was cleared with centrifugation at 1000 rpm prior to treating osteosarcoma cells.

Animal studies

All animal studies carried out in this study were done with the approval of the Institutional Animal Care and Use Committee of the Research Institute at Nationwide Children's Hospital (IACUC protocol AR15-00022) prior to conducting experiments. Six- to eight-week-old female C57BL/6 (for F420; RRID: MGI:2159769), BALB/c (for K7M2; RRID: IMSR_APB:4790), and CB17-SCID (for human OS-17 xenograft- CB17SC scid-/- (RRID: IMSR_TAC:cb17sc)) mice were used for all studies. For generation of primary tumors, single cell suspensions of $5x10^5$ cells were injected intra-tibially. Primary tumors were excised once they grew to 800 mm^3. For generation of experimental metastasis, F420 ($5x10^5$), K7M2 ($5x10^5$), or OS-17 ($1x10^6$) cells were inoculated intravenously via tail vein. Mice were followed until designated endpoint of experiment or until arriving at humane endpoint. For nintedanib (MedChemExpress, HY-50904) treatment, experimental metastasis was induced as described above. Two days after injection, mice were randomized to receive vehicle (0.5% Hydroxyethylcellulose, Eisen-Golden Laboratories, EG-HEC-3) or nintedanib 50 mg/kg twice per day. Mice were monitored and once an ill mouse (control for all three models) was confirmed to have lung metastasis, all vehicle and nintedanib treatment mice were sacrificed. All mice were euthanized by IACUC approved CO_2 inhalation method prior to processing as described below.

Tissue dissociation, single cell RNA library preparation and sequencing

Lungs harvested from mice were processed using the human tumor dissociation kit (Miltenyi Biotec, 130-095-929) with a GentleMacs Octo Dissociator with Heaters (Miltenyi Biotec, 130-096-427). Following dissociation into single cell suspension, single-cell 3' RNA-Seq libraries were prepared using Chromium Single Cell 3′RNA-sequencing system (10X Genomics) with the Reagent Kit v3.1 (10X Genomics, PN-1000121) according to the manufacturer's instructions. cDNA library quality and quantity were determined using an Agilent 2100 bioanalyzer using the High Sensitivity DNA Reagents kit (Agilent, 5607-4626) and then sequenced on an Illumina NovaSeq 6000. Raw data and initial processing was performed using cellranger version 7 (10X Genomics) with reads mapped to mm10 and hg19 versions of the mouse and human genomes.

Single-cell RNA sequencing analysis

10X data was loaded into Seurat toolkit version V4 for further analysis [16]. Cells with <200 detected genes or mitochondrial DNA >20% were removed. RNA counts were normalized with regularized negative binomial regression via SCTransform. After dimensionality reduction with principal component analysis and UMAP embedding, unsupervised clustering was achieved using “FindNeighbors” and “FindClusters” function in Seurat with dimensions 1:30 and resolution of 0.3 clustering of all cells and 0.5 for subclustering. Differential gene expression between clusters was determined using FindMarkers (Seurat) and the Wilcox method. Cell types were approximated with SingleR using the Human Lung Cell Atlas and the Human Primary Cell Atlas as references [17, 18]. Cell clusters were then curated manually based on the automated assignments and review of canonical marker expression.

Human normal lung samples were obtained from the Human Lung Cell Atlas, with samples filtered using the accompanying metadata to isolate cells from healthy lungs, nonsmokers, lung parenchyma, and then downsampled in a weighted fashion to include similar proportions of whole cell and nuclear libraries as the lung metastasis samples [17].

Differentially expressed genes were evaluated by GSEA against KEGG, GO:Molecular Function, GO:Biological Processes, and transcription factor activity (all from migdb) using fgsea [19]. Results were plotted in R using the ggplot suite.

Histology and Immunohistochemistry

Sternotomy was performed and lungs were flushed via slow instillation of phosphate buffered saline (PBS) (Corning, 21-031-CV) through right ventricle until lungs were cleared of blood. Lungs were dissected from mouse *en bloc* along with trachea and heart. Lungs were slowly instilled with 10% neutral buffered formalin (NBF) (Sigma-Aldrich, HT5012-1CS) until fully expanded, then trachea was tied off with suture and placed in NBF for 24 hours at 4°C. After repeated washing in PBS, lung lobes were carefully dissected from each other and processed for paraffin embedding (FFPE) or immunohistochemistry frozen (IHC-F). For FFPE, 4µm sections were deparaffinized with xylene and rehydrated through ethanol series. For cryosections, lung lobes were cryoprotected through a sucrose gradient (10%, 15%, 30%), mounted in Optimum Cutting Temperature compound, frozen in liquid nitrogen and then sectioned to 10µm. To quantify metastasis burden, FFPE sections were counterstained with hematoxylin and eosin via conventional methods. Heat-mediated antigen retrieval methods utilized citrate buffer (CB; pH 6.9) or Tris-EDTA buffer (TE; pH 9) with Tween 20 (Fisher Bioreagents, BP337-100) at 0.2% v/v. Antigen retrieval (AR) buffer used was antibody dependent (see below).

Immunofluorescence and microscopy

FFPE sections were rehydrated in PBS for 30 minutes. Human tissue sections utilized in this study were obtained from Nationwide Children's Pathology department under institutional review board approved study (IRB1100478). Cells growing on #1.5 glass coverslips (Electron Microscopy Sciences, 72204-04) were fixed in NBF for 10 minutes at room temperature. Following three rinses in PBS, coverslip or histological sections were then incubated for at least 1 hour in blocking solution consisting of PBS, 0.2% triton100 (v/v) (Sigma, X-100-100ml), and 3% bovine serum albumin (w/v) (Sigma, A-7888) at room temperature. Primary antibodies used: rabbit anti-fibronectin (Abcam, ab2413, AR=TE), rabbit anti-mouse SFTPC (Abcam, ab211326, AR= CB or TE), Arg1 (Cell Signaling Technology (CST), 93668, AR=CB), rabbit anti-mouse Ly6G (CST, 87048, AR=CB), hamster anti-Podoplanin (Developmental Studies Hybridoma Bank(DSHB), 8.1.1, AR=TE), rat anti-KRT8 (DSHB, TROMA-I, AR=TE), rat anti-Ki67 (Invitrogen, 14-5698-82, AR=CB), rat anti-mouse MHCII (Invitrogen, 14-5321-82, IHC-F), rabbit anti-human SFTPC (Millipore, ABC99, AR=TE), goat anti-Mrc1/Cd206 (R&D, AF2535, AR=CB), mouse anti-human fibronectin (R&D,MAB1918, AR=TE), rabbit anti-mouse Cd68 (R&D, MAB101141, AR= CB or TE), rabbit anti-mouse Cd68 AlexaFluor 488 (R&D, IC101141G, AR= CB or TE). Primary antibodies were diluted in blocking solution and sections were incubated in primary antibody solution overnight at 4°C. Following three rinses in PBS, sections were incubated with appropriate AlexaFluor labeled secondary antibodies (Invitrogen), DAPI (Invitrogen, D1306), and where indicated, Phalloidin AlexaFluor 647 (Invitrogen, A12379) or Wheat Germ Agglutinin (WGA) AlexaFluor 647 (Invitrogen, W11261) diluted in blocking solution for 1 hour at room temperature.

Following PBS rinses, coverslips and tissue sections were mounted in Fluoromount G (Invitrogen, 00495802).

Microscopy and image analysis

Fluorescent microscopy images were obtained on a LSM 800 confocal microscope using 20X air or 63X oil objectives. Tile-scanning was used for high-resolution imaging of large areas with images stitched together with 10% overlap using ZenBlue software. CZI files were then uploaded and processed using ImageJ. All manipulation of images (brightness/contrast and smoothing) were done uniformly to each image. For quantifying Krt8 and fibronectin fluorescence, samples were processed and imaged simultaneously under same microscope settings, then identical manual threshold was applied to all images in ImageJ. Fluorescence was measured/area with “measure” analysis function. Krt8 expression was normalized to Krt8 fluorescence in areas without visible metastases. Macrophage density was measured by first thresholding images then applying ‘Analyze particles’ function with area of 10µm^2 minimum and 0-1 circularity. The cell counter plugin was used to manually quantify Ki67+/ Sftpc+ cells, Ly6G+ neutrophils, or CD68+ macrophages. Metastasis burden was quantified from H/E sections by blinded examiner using Aperio ImageScope Software (V12.4.3). Whole lung lobe images were obtained with Aperio FL ScanScope digital slide scanner with 20X objective.

Statistical analysis

Statistical analysis for animal and bench studies was performed using Graphpad Prism V9. The number of samples and mice are explicitly stated in text with appropriate statistical test and p-values. Data reported with error bars represent mean +/- standard

error of the mean (SEM). Statistical analyses of the sequencing data are described in the relevant sections.

Data availability and resource sharing

Code used to analyze single cell RNA-seq (scRNA-seq) data can be found on GitHub at github.com/kidcancerlab/epithelial. Previously unpublished raw sequencing data is and the associated count tables with metadata is available through GEO at GSE252703. Cell lines utilized in this study are available from commercially available resources or can be obtained upon request to corresponding author.

Results

Disseminated osteosarcoma cells localize to alveolar epithelial niche and disrupt alveolar architecture during metastatic progression.

We first sought to determine the spatial localization of osteosarcoma cells as they begin to colonize the lung, which would provide evidence for the specific lung environment most relevant to these earliest steps in metastatic colonization. To control the timing of dissemination, we inoculated immunocompetent C57/Bl6 mice intravenously (tail vein) with F420 murine osteosarcoma cells. We then collected lungs from mice euthanized at 1, 7, and 14 days after injection and processed lungs onto slides to evaluate the development of the earliest metastatic niche. F420 cells demonstrated a stereotyped pattern of lung colonization characterized by extravasation and invasion through the alveolar epithelial layer, inducing injury to podoplanin (PDPN)+ type 1 alveolar epithelial cells (AEC1). We identified a compensatory increase of surfactant protein C (Spc)+ type 2 alveolar epithelial cells (AEC2) over areas of injured AEC1 (Figure 1A), reminiscent of

the process triggered by other types of alveolar injury [20] . Similar results were seen in the K7M2 murine osteosarcoma model (Supplemental Figure 1A).

In other nonmalignant models of alveolar injury, disruption of alveolar integrity promotes neutrophil followed by macrophage infiltration into the lung [21]. We likewise observed a short burst of neutrophil infiltration shortly after colonization that diminished over time and was followed by a significant and sustained accumulation of macrophages, mirroring the kinetics of immune infiltration observed in other alveolar injury models (Supplemental Figure 1B, REF [21]). Taken together, these data suggested that disseminated osteosarcoma cells colonize the distal alveolar niche and induce an acute lung injury response during early metastatic colonization.

To understand how these changes affect the behavior of the surviving osteosarcoma cells and the surrounding lung tissues, we isolated early F420 and K7M2 metastases using a stereomicroscope and processed them for single-cell RNA sequencing (scRNA-seq; Figure 1B). Cell cluster annotation was done using a combination of automated and manual approaches using established markers (Supplemental Figure 2A;C, methods). Multiple cell populations demonstrated enrichment in metastasis when compared to non-tumor bearing control lung tissues (Figure 1C, Supplemental Figure 2B). We divided cells computationally into infiltrating/immune and native/stromal compartments to quantify the relative frequencies of each distinct cell population. Doing this, we found that metastasis bearing lungs exhibit a marked enrichment in infiltrating myeloid cells (particularly macrophages) and distal airway epithelial cells (Figure 1D-E). Immunofluorescence imaging confirmed that developing metastases become highly enriched in macrophages and distal airway epithelial cells when compared to uninvolved lung (Supplemental Figure

2D-E). We therefore isolated the alveolar epithelial cells and macrophages to evaluate the phenotypic changes in the two most clearly altered stromal and immune cell populations, hypothesizing that the invasion of the osteosarcoma cells influences these changes, and that these constitute important elements of tumor education within the developing metastatic niche.

Metastasis associated epithelial cells adopt a non-healing wound phenotype

Distal epithelial cell clusters from metastases and healthy (non-metastasis bearing) C57BL/6 (control for F420) or BALB/c (control for K7M2) mice were merged, integrated, and re-analyzed through our Seurat-based pipeline. Several populations of epithelial cells were enriched in metastasis bearing lungs compared to control (Figure 2A). Five distal epithelial clusters were identified in F420 and K7M2 metastases, each with distinct gene expression signatures (Figure 2B).

To ensure that these findings reflect biology that is relevant to the human disease, we collected tissue samples from patients undergoing metastatectomy at our local institution and performed single-cell sequencing using the same protocol. To enhance the power of this analysis and ensure the broad applicability of these findings, we combined these with previously published datasets containing both normal lung tissues and metastatic osteosarcoma lesions [17, 18, 22-24]. This assessment of human tissues revealed changes in both epithelial content and phenotype, very similar to those observed in our murine models, with several epithelial cell clusters enriched in metastasis relative to healthy lung (Figure 2C-D).

AEC1 and AEC2 populations were discernible based on the enrichment of genes such as *Ager*, *Hopx* and *Sftpc* respectively. Two additional AEC2-like populations were found within the metastatic samples, one of which expressed genes such as *Lcn2* and *Lrg1* while the other demonstrated upregulation of genes involved in cell cycle such as *Mki67* and *Cdk1*. This finding was consistent with the physiologic reaction to alveolar injury, as AEC2 cells are facultative stem cells within the alveolus, functioning to re-establish epithelial barrier integrity after AEC1 injury [20]. In the canonical wound healing process, AEC2 are activated into a 'primed' pAEC2 state by AEC1 injury [25]. pAEC2 then enter the cell cycle (cAEC2) before differentiating into AEC1 cells to re-establish alveolar epithelial integrity. Given their phenotypic resemblance of these previously-defined subtypes, we assigned the *Lcn2*$^{+}$ population a label of 'primed' AEC2 (pAEC2) and the *Mki67*$^{+}$ cluster a label of 'cycling' AEC2 (cAEC2), consistent with the established literature for murine lung injury models [25]. We confirmed these sequencing findings in tissue slices by showing that AEC2 within the developing metastatic niches were hyperproliferative (Ki67+) relative to AEC2 in uninvolved areas of the lung across multiple models of osteosarcoma metastasis (Figure 2E-F). We concluded from these data that metastasis induces activation and proliferation of AEC2 within the metastatic niche, likely as one element of a physiologic wound-healing program triggered by metastatic invasion.

The fifth epithelial cluster demonstrated upregulation of atypical cytokeratins, such as *Krt8* and *Krt18/19*, and genes such as *Cdkn1a*, *Sfn*, and *Nupr1.* This was an interesting finding, as Krt8^{+} is a primary marker of a recently described fibrogenic intermediate produced as activated AEC2 cells differentiate into AEC1 cells in response to injury [25-27]. Under normal conditions, these intermediates are short-lived and do not persist beyond the

acute phase of the injury. However, under certain chronic inflammatory conditions, these damage associated transient progenitors (DATP) (also referred to as alveolar differentiation intermediates (ADI) and pre-alveolar type-1 transitional cell state (PATS)) become arrested in the Krt8+ transitional state and can promote pathologic fibrosis. Indeed, a similar process has been shown to occur in human patients with chronic idiopathic pulmonary fibrosis [25-27]. We confirmed that this accumulation of metastasis-associated Krt8+ epithelial cells occurs across multiple osteosarcoma models (Figure 2G-H).

Of note, in human lung pathologic conditions, AEC2 have been shown to differentiate through a disease-specific, aberrant KRT17+ basaloid cell state. These KRT17+ cells stain positive for KRT8 by immunohistochemistry (IHC) and cluster with murine Krt8+ DATP in cross-species single-cell transcriptomic analyses [27, 28]. Thus, they are likely to be an orthologous AEC intermediate. Our human osteosarcoma metastasis data sets replicated the finding in the murine models, with strong enrichment of KRT17+ basaloid cells (Figure 2C). To validate this observation, we showed that KRT8+ AEC intermediates were prevalent within human lung metastasis samples by immunofluorescence (Supplemental Figure 3). These findings demonstrate that basaloid/DATP accumulation is a conserved phenomenon in osteosarcoma metastasis and not unique to mouse models. We conclude that partially differentiated epithelial intermediates, which have been associated with aberrant non-healing lung wounds in other pathological processes, consistently accumulate within the developing metastatic niche in both mice and humans. Functionally, this finding suggested that impaired epithelial wound healing is central to osteosarcoma lung metastasis. As lung alveolar wound repair is a highly stereotyped and

regulated process that requires coordination with other cell types (such as fibroblasts and macrophages [29]), we wondered whether the monocyte-derived macrophages that accumulate around developing metastatic lesions might evidence changes characteristic of either physiologic or pathologic wound healing. We thus leveraged our single-cell datasets to define the macrophage phenotypes associated with osteosarcoma metastasis.

Metastasis associated macrophages are enriched in scar, chronic wound-like phenotype that are spatially segregated in osteosarcoma metastasis

Macrophages can play paradoxical roles during distinct phases of wound healing [30]. In the early wound healing response, macrophages are predominantly inflammatory in nature [31, 32], marked by high expression of antigen presentation proteins and inflammatory cytokines in the early phases of wound healing [33]. Once the inciting noxious stimulus is controlled, anti-inflammatory/resolution macrophages promote healing by reorganizing the extracellular matrix, phagocytosing apoptotic cells, and dampening inflammation, though their uncontrolled accumulation can promote chronic, non-healing wounds [34].

To ascertain the macrophage phenotypes associated with developing osteosarcoma metastases, we isolated myeloid cells from our murine and human scRNA-seq datasets. In this analysis, we also included primary murine tibial tumors to define how the surrounding microenvironment impacts macrophage phenotypes in the primary vs. metastatic microenvironment. Murine osteosarcoma metastases demonstrated marked accumulation of several macrophage populations that were transcriptionally distinct from populations present in healthy lung and tibial tumors (Figure 3A-B). Tumor associated

macrophage annotations were made using recently published criteria [35]**.** Notably, a population of macrophages expressing *Trem2*, *Cd9*, *and Spp1* were highly enriched in lung metastasis compared to healthy lung and primary tibial tumors. This macrophage population shares transcriptional profile with scar-like macrophages, a macrophage phenotype identified as a crucial driver of pathologic fibrosis within the lung and during liver metastasis [36-38]. Their enrichment in osteosarcoma lung metastasis, but not in primary tibial tumors, suggests a microenvironmental influence on macrophage phenotypes, with chronic injury/fibrosis being promoted specifically in the lung, likely secondary to osteosarcoma-induced aberrant wound healing process. Similar macrophage subpopulations were enriched in human osteosarcoma metastasis relative to healthy human lung (Figure 3C-D).

Given that macrophage phenotypes are driven by surrounding microenvironmental cues, we utilized immunofluorescence to ascertain the spatial organization of distinct macrophage subpopulations in both osteosarcoma metastases and normal lung. Inflammatory, acute wound macrophages can be identified via high expression of MHC II proteins whereas chronic wound, fibrotic macrophages can be identified by Cd206 (Mrc1) or Arginase 1 (Arg1) expression [32, 33, 39]. To ensure that stains were macrophage-specific, we co-stained these sections with Cd68 to label all bona fide macrophages. Macrophage subsets demonstrated a striking spatial segregation in both immunocompetent models. Acute wound-like inflammatory macrophages (MHC II +) were confined to the metastasis:lung border while chronic wound-like, pro-fibrotic macrophages (Cd206 or Arg1 +) were concentrated within core of the metastatic lesion (Figure 3E-F).

Based on our epithelial and macrophage data, we propose a model wherein the activation of epithelial wound healing, triggered by the infiltrating osteosarcoma cells at the initial stages of metastasis and continuing along the leading edge during lesional growth, coincides with the enrichment of inflammatory macrophages. Subsequently, the tumor-educated inability to resolve the wound causes macrophages with chronic wound phenotypes to accumulate within the metastatic lesion (Figure 3G). In other disease states, this chronic wound healing process ultimately leads to pulmonary fibrosis, characterized by the pathological deposition of extracellular matrix proteins such as fibronectin [40]. Therefore, we next investigated if osteosarcoma metastases are fibrogenic.

Osteosarcoma cells co-opt epithelial:mesenchymal interactions to promote fibrotic reprogramming of metastasis associated lung

Fibronectin is an extracellular matrix protein that is necessary for proper wound healing but can promote progressive organ dysfunction if not tightly regulated [41]. In all three of our osteosarcoma models tested, fibronectin markedly accumulated within developing metastatic lesions, relative to adjacent unaffected lung. Given the findings above, this is consistent with a metastasis-induced fibrotic transformation of the osteosarcoma associated lung (Figure 4A). To elucidate whether osteosarcoma-associated fibronectin deposition is metastasis-specific, we compared primary F420 and K7M2 tibial tumors to lung metastases. Primary tibial tumors expressed low levels of intracellular fibronectin while metastases were characterized by extensive extracellular, fibrillar fibronectin matrices, suggesting that fibronectin matrix formation is metastasis specific and not an inherent trait of osteosarcoma tumors (Figure 4B).

In non-malignant lung fibrosis diseases, activated myofibroblast secrete and organize fibronectin into dense matrices [42]. In lung fibrotic disorders, epithelial damage triggers fibroblast activation and fibrosis [43]. Fibronectin deposition by cancer associated fibroblasts is also noted in other tumor types [44]. However, our scRNA-seq data did not demonstrate enrichment of myofibroblasts in osteosarcoma metastases, suggesting an alternative source of fibrotic matrix in osteosarcoma metastases. Given that this tumor type is a sarcoma, developmentally related to fibroblasts and with strong matrix-forming tendencies, we leveraged the xenogeneic nature of the OS-17 metastasis model to help determine whether metastasis-associated fibronectin is tumor-cell derived. To do this, we stained metastatic lesions with a human-specific fibronectin antibody. Interestingly, human (tumor) derived fibronectin was highly enriched in areas with dense collections of Krt8+ DATP cells (Figure 4C).

This spatial relationship between epithelial cells and osteosarcoma-derived fibronectin suggested that epithelial cells could initiate osteosarcoma fibronectin deposition, in a process analogous to the epithelial:fibroblast interactions that have been shown to promote lung fibrosis and to the carcinoma:fibroblast interactions that have been shown to promote metastasis in other tumor types [45, 46]. To test this hypothesis within a reductionist system, OS-17 cells were co-cultured with human immortalized lung epithelial cells (HBEC) or stimulated with epithelial conditioned media. OS-17 cells generated a complex fibronectin matrix in the presence of lung epithelial cells (Figure 4D). This reaction was replicated by stimulation with epithelial-conditioned media (Figure 4E), suggesting that the reaction is triggered by soluble signals produced by the epithelial cells. Interestingly, epithelial cells did not induce fibronectin matrix deposition in a poorly

metastatic cell line (OS-25), suggesting that lung-induced fibronectin matrix deposition is dictated by tumor intrinsic traits (Supplemental Figure 4A) which may be associated with metastatic capacity.

In summary, chronic unresolved injury induced by osteosarcoma lung colonization culminated in microenvironmental fibrosis. This fibronectin-rich matrix was synthesized by osteosarcoma cells in a metastasis-dependent manner due to microenvironment specific epithelial interactions. We thus hypothesized that osteosarcoma-induced chronic injury and subsequent fibrotic transformation of the lung niche are key drivers of osteosarcoma metastasis progression and that inhibiting this metastasis-associated fibrosis would prevent osteosarcoma metastasis growth.

Nintedanib, an anti-fibrotic tyrosine kinase inhibitor, slows metastasis growth

Fibrotic lung conditions are progressive, often fatal diseases. Nintedanib is an orally available tyrosine kinase inhibitor with a broad target profile that has demonstrated clinical efficacy in slowing the progression of fibrotic lung diseases [47-49]. The pathophysiological overlap with osteosarcoma metastases and lung fibrotic conditions suggested that anti-fibrotic agents such as nintedanib could disrupt metastasis progression. To test the effect of nintedanib on osteosarcoma metastasis progression, tumor cells were injected intravenously via tail vein to promote experimental metastasis formation. Nintedanib or vehicle was initiated two days after injection to ensure nintedanib was not affecting extravasation into lung (Figure 5A). Study mice were monitored daily for signs of metastasis. When metastasis was confirmed in one mouse, all mice were humanely euthanized and lung metastases quantified (Figure 5B-G). We found that nintedanib significantly hindered metastatic progression in both immunocompetent (F420

and K7M2) and immunodeficient (OS-17) models. The conserved activity of nintedanib in disrupting metastasis progression across models and within three distinct mouse strains strongly supports the anti-metastatic effect in osteosarcoma, likely through a disruption of this pathologically aberrant wound-healing process.

Nintedanib prevents osteosarcoma induced chronic wound phenotype

We next sought insights as to the mechanisms underlying the effects of nintedanib on osteosarcoma lung metastasis through pharmacodynamic analysis of fibrosis markers. As proof-of-principal, we found that nintedanib, while not overtly cytotoxic to osteosarcoma cells, significantly inhibited epithelial induced fibronectin deposition *in vitro* (Supplemental Figure 4B). Because nintedanib had a potent effect on preventing osteosarcoma progression, we treated mice with established metastatic lesions to understand how nintedanib reprograms the metastatic microenvironment *in vivo*. We focused specifically on fibronectin deposition and the accumulation of fibrosis associated epithelial cells (Krt8) and macrophages (Cd206 and Arg1). Nintedanib treatment significantly decreased fibronectin accumulation and reduced both Krt8+ DATP as well as Cd206+ and Arg1+ chronic wound-like macrophages compared to vehicle treated F420 metastases (Figure 5H-K for quantitation; Supplemental Figure 4C for representative images). Collectively, the results of our preclinical nintedanib trial coupled with this pharmacodynamic analysis of nintedanib-treated metastases and the results of the *in vitro* studies suggest a tight linkage between the anti-metastatic activity and the anti-fibrogenic activity of nintedanib. These results also suggest a requirement for fibrotic reprogramming of the lung microenvironment during osteosarcoma metastasis progression. Inhibition of this fibrogenic, aberrant wound healing program represents a

novel therapeutic vulnerability with potential for combatting osteosarcoma lung metastasis.

Discussion

How disseminated cancer cells colonize, integrate with, and coerce foreign organs to promote metastatic growth remains a poorly understood phenomenon. With respect to osteosarcoma, specifically, our data supports a model wherein the tumor cells trigger and then perpetuate the lung's intrinsic wound healing program, beginning with dissemination and resulting in a chronic, non-healing fibrotic wound. The characterization of a tumor as a non-healing wound is not new. It was first postulated by Virchow, then further conceptualized by Dvorak. However, this paradigm largely focused on tumorigenesis of primary tumors in adult epithelial carcinomas [50]. Our results demonstrate that osteosarcoma, a mesenchymal pediatric tumor, induces alveolar epithelial injury upon colonization of the lung, leading to a chronic non-healing wound and fibrotic transformation of the surrounding lung. In many ways, osteosarcoma-epithelial interactions mimic, albeit in a highly pathological sense, epithelial-lung fibroblast interactions that occur during non-malignant lung wounds [43, 51]. This observation may suggest that aberrant epithelial-mesenchymal interactions are central mechanisms that drive lung metastasis across diverse histological subtypes.

Indeed, an analogous scenario has been demonstrated in breast cancer lung metastasis, wherein epithelial tumor cells co-opt and activate normal lung mesenchymal fibroblasts to drive metastasis, with fibrogenic wound-like processes playing a central role in the mechanisms for colonization [52]. It may be that in the case of breast cancer metastasis, the tumor cells play the role of the epithelial cells and the fibroblasts the role of the

mesenchymal cell in a process similar to that observed here. If true, this aberrant wound healing process and the resulting fibrogenic changes may represent mechanisms broadly conserved. Notably, organs with facultative repair capacity that are susceptible to fibrosis, such as the lung, liver, and pancreas, are organs commonly affected by high metastatic rates (or, in the case of the pancreas, characterized by fibrotic/desmoplastic primary tumors) [8, 53, 54]. It will be critical from a therapeutic perspective to elucidate whether initiation of abnormal wound healing and progression to organ fibrosis is specific to a handful of histological tumor types or a generalizable mechanism.

Our work significantly advances the mechanistic understanding of osteosarcoma lung metastasis. Our findings converge on previous findings by Zhang and colleagues but add several critical observations [55]. Notably, our work demonstrates that fibrogenic reprogramming is a niche wide event initiated by osteosarcoma-epithelial interactions and provides critical pharmacodynamic analysis of nintedanib treated metastases in an immunocompetent host. Our mechanisms also unify and advance concepts emerging from other recent publications, suggesting that cancer cells disrupt the physiology of the lung epithelia during colonization [56, 57].

Long considered background bystanders in the processes that facilitate malignant progression, stromal cells such as alveolar epithelial cells have received relatively little attention as potential drivers of metastasis biology. However, our work amplifies the warning that these cells should not be overlooked. Indeed, the clear physical proximity of early disseminated osteosarcoma cells to alveolar epithelial cells and the functional data demonstrating that epithelial cells initiate fibrogenic reprograming of osteosarcoma cells strongly suggest active paracrine two-way signaling between osteosarcoma cells and

epithelial cells as a key event driving osteosarcoma colonization of the lung. Future work is required to clarify the mediators of these osteosarcoma-epithelial interactions.

Elucidating why fibronectin/fibrosis is required for osteosarcoma metastatic progression remains an important area of ongoing investigation. Potential, non-mutually exclusive mechanisms include: directly providing survival signals to tumor cells during early lung colonization [58], resistance to chemotherapy [59, 60], protection against innate/adaptive anti-tumor immunity [61], and reprogramming of niche cells such as macrophages. We note that effectiveness of nintedanib was similar in mice with or without intact adaptive immunity, which does not rule out an important role for fibrosis in controlling anti-tumor immunity, but does support the idea that fibronectin/fibrosis could function through both tumor cell-intrinsic and non-tumor cell-intrinsic mechanisms to promote metastatic progression.

In conclusion, we note that metastases are complex multi-cellular structures composed of tumor, immune, and altered resident stromal cells. Utilizing scRNA-seq, we illuminate how osteosarcoma cells manipulate the lung microenvironment into a chronic state of wound healing. From a translational perspective, we demonstrate that targeting the microenvironment is a viable therapeutic option across multiple osteosarcoma models, which is an important consideration due to the substantial intertumoral heterogeneity inherent to osteosarcoma.

Acknowledgements

We would like to thank the patients and their families for donation of tissue. We would like to thank the Histopathology, Microscopy, Biopathology Center Processing and Banking,

and Institute for Genomic Medicine sequencing cores at Nationwide Children's Hospital for their technical assistance. This work is supported by NIH R01CA260178 (RDR), Translational Studies Grant from the Osteosarcoma Institute (RDR), CancerFree KIDS Foundation (RDR, JBR), Steps For Sarcoma Foundation (RDR,JBR), Sarcoma Foundation of America (RDR), Nationwide Children's Director's Strategic Development Fund (RDR), Alex's Lemonade Stand Crazy 8 Award (RDR,RD,BEG), Alex's Lemonade Stand Foundation Young Investigator Award (JBR), NIH CTSA Grant UL1TR002733 (RDR).

References

1. Welch, D.R. and D.R. Hurst, *Defining the Hallmarks of Metastasis.* Cancer Res, 2019. **79**(12): p. 3011-3027.
2. Massague, J. and K. Ganesh, *Metastasis-Initiating Cells and Ecosystems.* Cancer Discov, 2021. **11**(4): p. 971-994.
3. Schmidt-Kittler, O., et al., *From latent disseminated cells to overt metastasis: genetic analysis of systemic breast cancer progression.* Proc Natl Acad Sci U S A, 2003. **100**(13): p. 7737-42.
4. Hu, Z. and C. Curtis, *Looking backward in time to define the chronology of metastasis.* Nat Commun, 2020. **11**(1): p. 3213.
5. Hu, Z., et al., *Multi-cancer analysis of clonality and the timing of systemic spread in paired primary tumors and metastases.* Nat Genet, 2020. **52**(7): p. 701-708.
6. Klein, C.A., *Cancer progression and the invisible phase of metastatic colonization.* Nat Rev Cancer, 2020. **20**(11): p. 681-694.
7. Altorki, N.K., et al., *The lung microenvironment: an important regulator of tumour growth and metastasis.* Nat Rev Cancer, 2019. **19**(1): p. 9-31.
8. Kotton, D.N. and E.E. Morrisey, *Lung regeneration: mechanisms, applications and emerging stem cell populations.* Nat Med, 2014. **20**(8): p. 822-32.
9. Plantier, L., et al., *Physiology of the lung in idiopathic pulmonary fibrosis.* Eur Respir Rev, 2018. **27**(147).
10. Hardie, W.D., S.W. Glasser, and J.S. Hagood, *Emerging concepts in the pathogenesis of lung fibrosis.* Am J Pathol, 2009. **175**(1): p. 3-16.
11. Langley, R.R. and I.J. Fidler, *The seed and soil hypothesis revisited--the role of tumor-stroma interactions in metastasis to different organs.* Int J Cancer, 2011. **128**(11): p. 2527-35.
12. Saraf, A.J., J.M. Fenger, and R.D. Roberts, *Osteosarcoma: Accelerating Progress Makes for a Hopeful Future.* Front Oncol, 2018. **8**: p. 4.

13. Roberts, R.D., et al., *Provocative questions in osteosarcoma basic and translational biology: A report from the Children's Oncology Group.* Cancer, 2019. **125**(20): p. 3514-3525.
14. Smeland, S., et al., *Survival and prognosis with osteosarcoma: outcomes in more than 2000 patients in the EURAMOS-1 (European and American Osteosarcoma Study) cohort.* Eur J Cancer, 2019. **109**: p. 36-50.
15. Fodstad, O., et al., *Characteristics of a cell line established from a patient with multiple osteosarcoma, appearing 13 years after treatment for bilateral retinoblastoma.* Int J Cancer, 1986. **38**(1): p. 33-40.
16. Hao, Y., et al., *Integrated analysis of multimodal single-cell data.* Cell, 2021. **184**(13): p. 3573-3587 e29.
17. Sikkema, L., et al., *An integrated cell atlas of the lung in health and disease.* Nat Med, 2023. **29**(6): p. 1563-1577.
18. Aran, D., et al., *Reference-based analysis of lung single-cell sequencing reveals a transitional profibrotic macrophage.* Nat Immunol, 2019. **20**(2): p. 163-172.
19. Korotkevich, G., et al., *Fast gene set enrichment analysis.* bioRxiv, 2021: p. 060012.
20. Barkauskas, C.E., et al., *Type 2 alveolar cells are stem cells in adult lung.* J Clin Invest, 2013. **123**(7): p. 3025-36.
21. Izbicki, G., et al., *Time course of bleomycin-induced lung fibrosis.* Int J Exp Pathol, 2002. **83**(3): p. 111-9.
22. Natri, H.M., et al., *Cell type-specific and disease-associated eQTL in the human lung.* bioRxiv, 2023.
23. Lukassen, S., et al., *SARS-CoV-2 receptor ACE2 and TMPRSS2 are primarily expressed in bronchial transient secretory cells.* EMBO J, 2020. **39**(10): p. e105114.
24. Zhou, Y., et al., *Single-cell RNA landscape of intratumoral heterogeneity and immunosuppressive microenvironment in advanced osteosarcoma.* Nat Commun, 2020. **11**(1): p. 6322.
25. Choi, J., et al., *Inflammatory Signals Induce AT2 Cell-Derived Damage-Associated Transient Progenitors that Mediate Alveolar Regeneration.* Cell Stem Cell, 2020. **27**(3): p. 366-382 e7.
26. Kobayashi, Y., et al., *Persistence of a regeneration-associated, transitional alveolar epithelial cell state in pulmonary fibrosis.* Nat Cell Biol, 2020. **22**(8): p. 934-946.
27. Strunz, M., et al., *Alveolar regeneration through a Krt8+ transitional stem cell state that persists in human lung fibrosis.* Nat Commun, 2020. **11**(1): p. 3559.
28. Jaeger, B., et al., *Airway basal cells show a dedifferentiated KRT17(high)Phenotype and promote fibrosis in idiopathic pulmonary fibrosis.* Nat Commun, 2022. **13**(1): p. 5637.
29. Plante-Bordeneuve, T., C. Pilette, and A. Froidure, *The Epithelial-Immune Crosstalk in Pulmonary Fibrosis.* Front Immunol, 2021. **12**: p. 631235.
30. Park, M.D., et al., *Macrophages in health and disease.* Cell, 2022. **185**(23): p. 4259-4279.
31. Shi, C. and E.G. Pamer, *Monocyte recruitment during infection and inflammation.* Nat Rev Immunol, 2011. **11**(11): p. 762-74.

32. Misharin, A.V., et al., *Monocyte-derived alveolar macrophages drive lung fibrosis and persist in the lung over the life span.* J Exp Med, 2017. **214**(8): p. 2387-2404.
33. Cheng, P., S. Li, and H. Chen, *Macrophages in Lung Injury, Repair, and Fibrosis.* Cells, 2021. **10**(2).
34. Aggarwal, N.R., L.S. King, and F.R. D'Alessio, *Diverse macrophage populations mediate acute lung inflammation and resolution.* Am J Physiol Lung Cell Mol Physiol, 2014. **306**(8): p. L709-25.
35. Ma, R.Y., A. Black, and B.Z. Qian, *Macrophage diversity in cancer revisited in the era of single-cell omics.* Trends Immunol, 2022. **43**(7): p. 546-563.
36. Yofe, I., et al., *Spatial and Temporal Mapping of Breast Cancer Lung Metastases Identify TREM2 Macrophages as Regulators of the Metastatic Boundary.* Cancer Discov, 2023. **13**(12): p. 2610-2631.
37. Fallowfield, J.A., et al., *Scar-associated macrophages are a major source of hepatic matrix metalloproteinase-13 and facilitate the resolution of murine hepatic fibrosis.* J Immunol, 2007. **178**(8): p. 5288-95.
38. Ramachandran, P., et al., *Resolving the fibrotic niche of human liver cirrhosis at single-cell level.* Nature, 2019. **575**(7783): p. 512-518.
39. Koh, T.J. and L.A. DiPietro, *Inflammation and wound healing: the role of the macrophage.* Expert Rev Mol Med, 2011. **13**: p. e23.
40. Yu, Q.Y. and X.X. Tang, *Irreversibility of Pulmonary Fibrosis.* Aging Dis, 2022. **13**(1): p. 73-86.
41. Upagupta, C., et al., *Matrix abnormalities in pulmonary fibrosis.* Eur Respir Rev, 2018. **27**(148).
42. Phan, S.H., *The myofibroblast in pulmonary fibrosis.* Chest, 2002. **122**(6 Suppl): p. 286S-289S.
43. Sakai, N. and A.M. Tager, *Fibrosis of two: Epithelial cell-fibroblast interactions in pulmonary fibrosis.* Biochim Biophys Acta, 2013. **1832**(7): p. 911-21.
44. Sahai, E., et al., *A framework for advancing our understanding of cancer-associated fibroblasts.* Nat Rev Cancer, 2020. **20**(3): p. 174-186.
45. Friedman, G., et al., *Cancer-associated fibroblast compositions change with breast cancer progression linking the ratio of S100A4(+) and PDPN(+) CAFs to clinical outcome.* Nat Cancer, 2020. **1**(7): p. 692-708.
46. Chapman, H.A., *Epithelial-mesenchymal interactions in pulmonary fibrosis.* Annu Rev Physiol, 2011. **73**: p. 413-35.
47. Flaherty, K.R., et al., *Nintedanib in Progressive Fibrosing Interstitial Lung Diseases.* N Engl J Med, 2019. **381**(18): p. 1718-1727.
48. Behr, J., et al., *Survival and course of lung function in the presence or absence of antifibrotic treatment in patients with idiopathic pulmonary fibrosis: long-term results of the INSIGHTS-IPF registry.* Eur Respir J, 2020. **56**(2).
49. Gunatilaka, A., et al., *Anti-fibrotic strategies and pulmonary fibrosis.* Adv Pharmacol, 2023. **98**: p. 179-224.
50. Dvorak, H.F., *Tumors: wounds that do not heal. Similarities between tumor stroma generation and wound healing.* N Engl J Med, 1986. **315**(26): p. 1650-9.
51. Zepp, J.A., et al., *Distinct Mesenchymal Lineages and Niches Promote Epithelial Self-Renewal and Myofibrogenesis in the Lung.* Cell, 2017. **170**(6): p. 1134-1148 e10.

52. Pein, M., et al., *Metastasis-initiating cells induce and exploit a fibroblast niche to fuel malignant colonization of the lungs.* Nat Commun, 2020. **11**(1): p. 1494.
53. Brodt, P., *Role of the Microenvironment in Liver Metastasis: From Pre- to Prometastatic Niches.* Clin Cancer Res, 2016. **22**(24): p. 5971-5982.
54. Whatcott, C.J., et al., *Desmoplasia in Primary Tumors and Metastatic Lesions of Pancreatic Cancer.* Clin Cancer Res, 2015. **21**(15): p. 3561-8.
55. Zhang, W., et al., *Adaptive Fibrogenic Reprogramming of Osteosarcoma Stem Cells Promotes Metastatic Growth.* Cell Rep, 2018. **24**(5): p. 1266-1277 e5.
56. Ombrato, L., et al., *Metastatic-niche labelling reveals parenchymal cells with stem features.* Nature, 2019. **572**(7771): p. 603-608.
57. Montagner, M., et al., *Crosstalk with lung epithelial cells regulates Sfrp2-mediated latency in breast cancer dissemination.* Nat Cell Biol, 2020. **22**(3): p. 289-296.
58. Barney, L.E., et al., *Tumor cell-organized fibronectin maintenance of a dormant breast cancer population.* Sci Adv, 2020. **6**(11): p. eaaz4157.
59. Deng, M., et al., *Extracellular matrix stiffness determines DNA repair efficiency and cellular sensitivity to genotoxic agents.* Sci Adv, 2020. **6**(37).
60. Pietila, E.A., et al., *Co-evolution of matrisome and adaptive adhesion dynamics drives ovarian cancer chemoresistance.* Nat Commun, 2021. **12**(1): p. 3904.
61. Boulter, L., et al., *The fibrotic and immune microenvironments as targetable drivers of metastasis.* Br J Cancer, 2021. **124**(1): p. 27-36.

Figures

Figure 1: Osteosarcoma lung colonization induces acute alveolar injury response

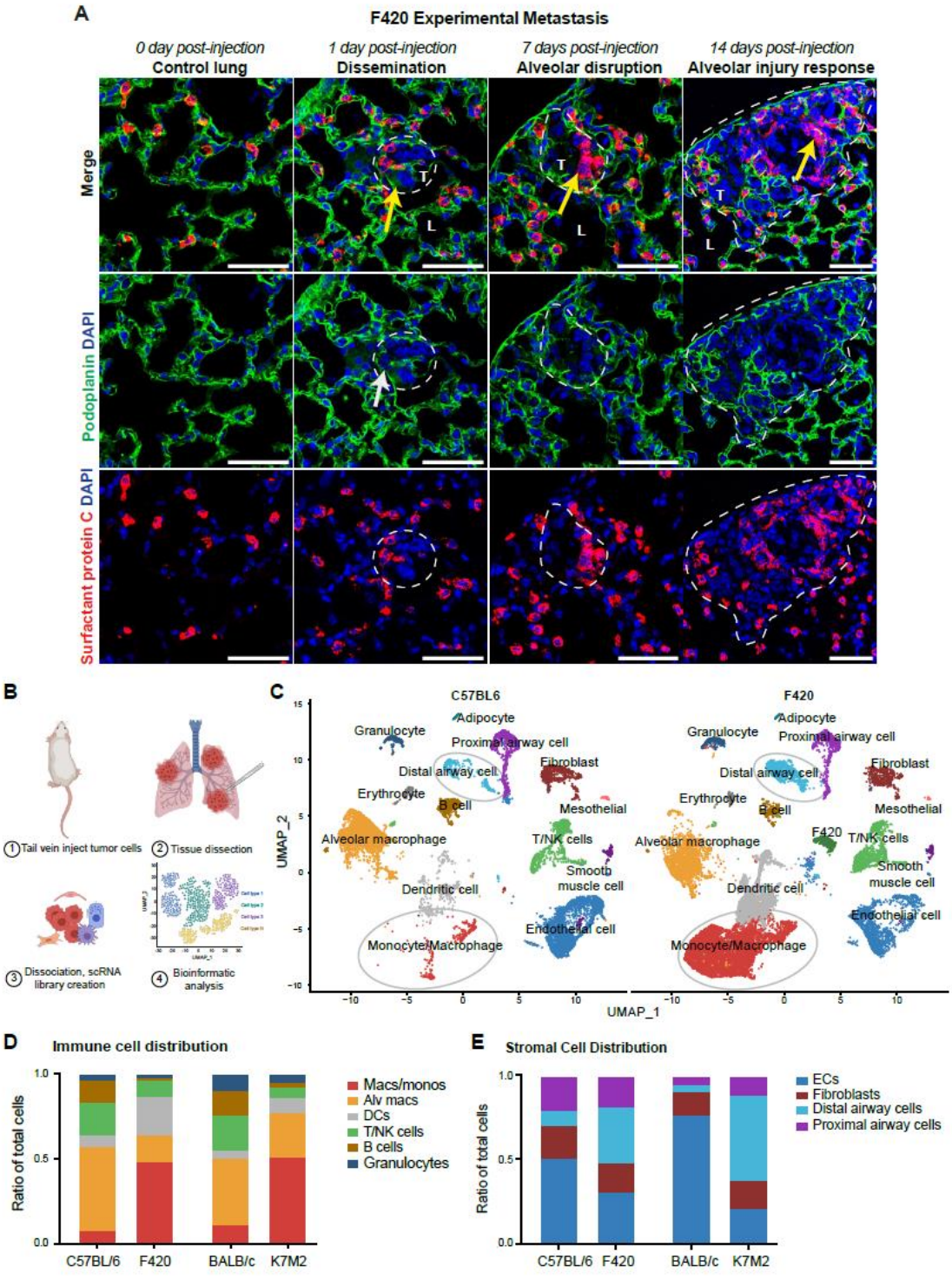

Figure 1:

Osteosarcoma lung colonization induces acute alveolar injury response. **A,** IHC of control lung and early metastatic lesions (marked by dash circle). White arrow denotes AEC1 (Podoplanin;green) injury while yellow arrow notes AEC2 response (Spc;red). Nuclei are counterstained with DAPI (blue). Scale bar= 50µm. **B,** Schematic for approach to metastasis scRNA-sequencing. **C,** Uniform manifold projection (UMAP) demonstrating cell clusters in non-metastasis bearing C57BL6 compared to F420 metastasis. Grey circles denote populations enriched in metastasis bearing lung **D-E,** Relative quantification of cell type distribution by scRNA-sequencing.

Figure 2: Metastasis associated epithelial cells acquire chronic wound phenotype

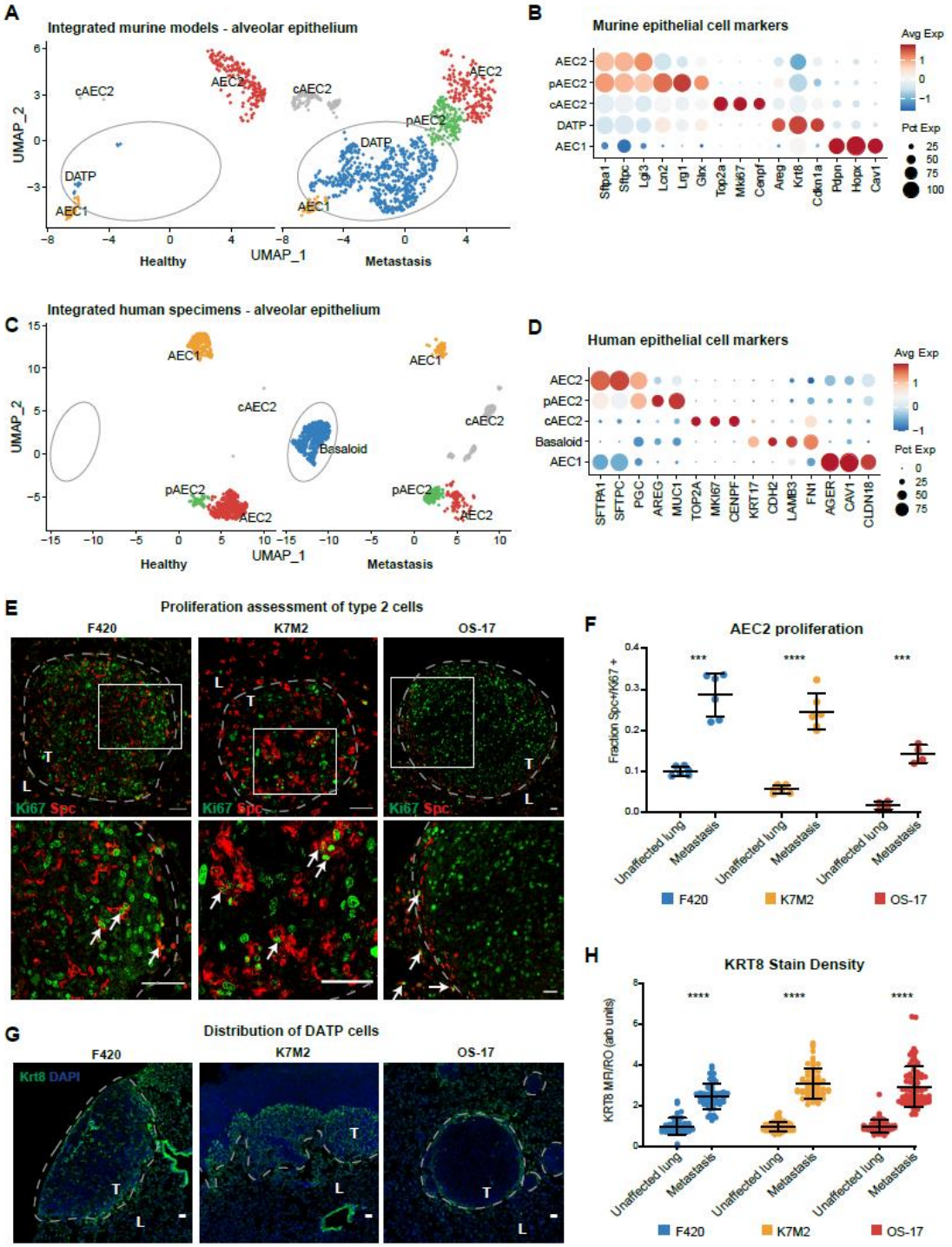

Figure 2:

Metastasis associated epithelial cells acquire chronic wound phenotype. **A,** UMAP plot of murine alveolar epithelial cells in healthy lung compared to metastasis. Grey circle denotes marked enrichment of DATP in metastasis. **B,** Dotplot demonstrating expression of key marker genes (columns) in alveolar epithelial cell clusters (row). **C,** UMAP plot of normal human lung specimens compared to patient lung metastasis samples. Grey circle denotes enrichment of basaloid cells in osteosarcoma metastasis. **D,** Dotplot demonstrating expression of key marker genes. **E,** IHC of Spc (red; AEC2 marker) and Ki67 (green; proliferation marker). L= unaffected lung, T= metastasis. Dash circle notes lung-metastasis border. Rectangle marks inset shown below. Areas demonstrate examples of Spc+Ki67+ cells. Nuclei are counterstained with DAPI (blue). Scale bar= 50µm. **F,** Quantification of AEC2 proliferation. 100 cells/animal, n=4. Welch's t-test: F420 p= 0.0003, K7M2 p= <0.0001, OS-17 p= 0.0004. **G,** IHC of Krt8 (DATP marker). Scale bar= 50µm. Nuclei are counterstained with DAPI (blue). Dash line notes lung-metastasis border. **H,** Quantification of DATP (by Krt8 fluorescence). N=4 animals, at least 10 regions of interest per animal for metastasis and unaffected lung. Welch's t-test: p=<0.0001.

Figure 3: Metastasis associated macrophages adopt wound-like phenotypes that are spatially segregated

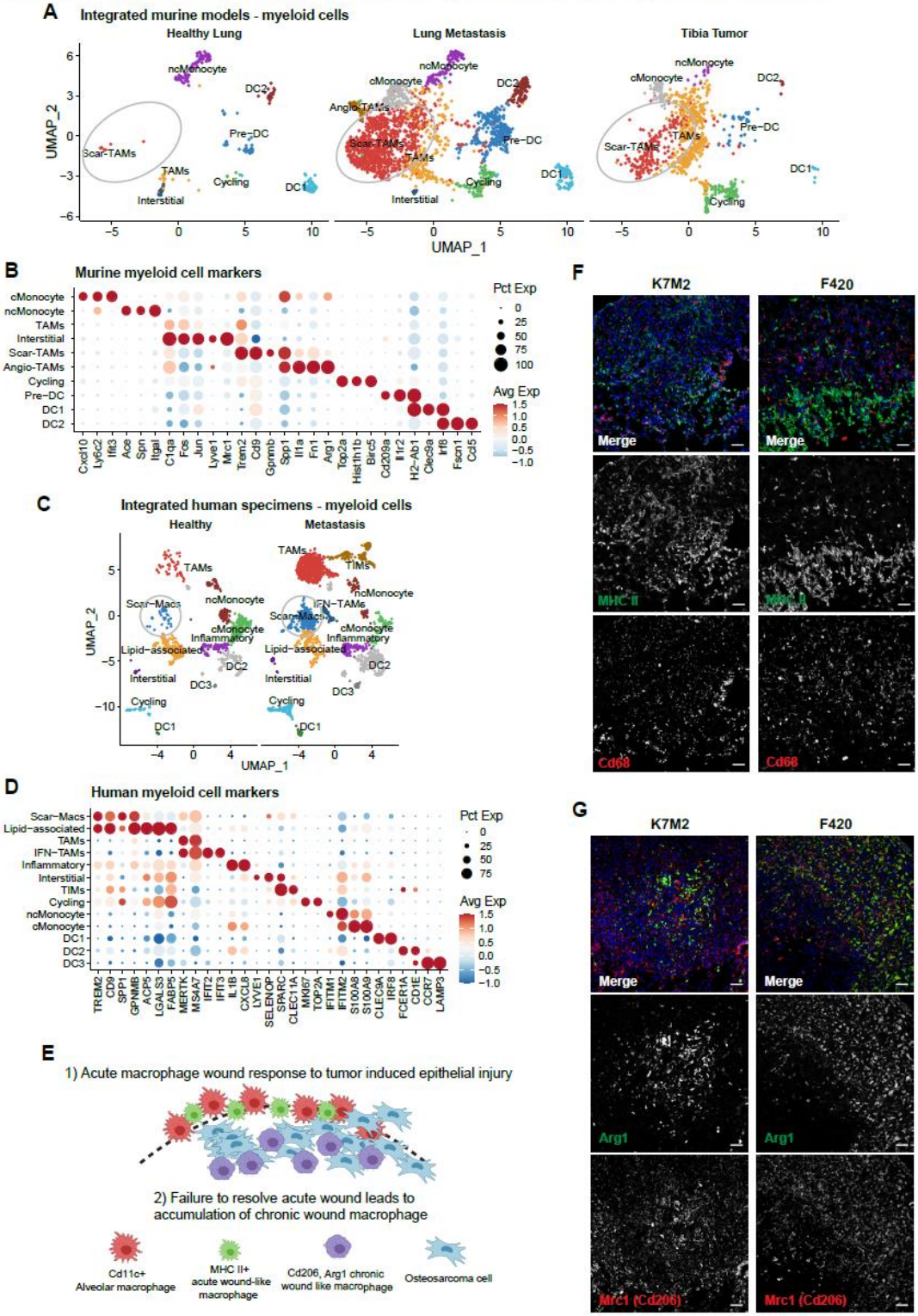

Figure 3

Metastasis associated macrophages adopt wound-like phenotypes that are spatially segregated. **A,** UMAP of myeloid cells including macrophages and dendritic cells in healthy lungs compared to F420 metastasis and F420 tibia tumor. Grey circle notes enrichment of scar macrophages in lung metastasis relative to tibia tumor and healthy lung. **B,** Dotplot demonstrating expression of key marker genes (columns) in myeloid cell clusters (row). **C,** UMAP plot of normal human lung specimens compared to patient lung metastasis samples. Grey circle denotes enrichment of scar macrophages in osteosarcoma metastasis. **D,** Dotplot demonstrating expression of key marker genes. **E-F,** IHC of K7M2 and F420 metastasis staining for acute wound macrophage (MHC II;green) and chronic wound macrophages (Arg1;green and Mrc1;red) demonstrating spatial enrichment of acute wound macrophages on tumor-lung border and chronic wound macrophages in metastasis core. Nuclei are counterstained with DAPI (blue). Scale bar= 50µm. **F,** Schematic model of macrophage subpopulations and their localization within osteosarcoma metastasis.

Figure 4: Lung epithelial cells induce metastasis-specific osteosarcoma fibronectin matrix formation

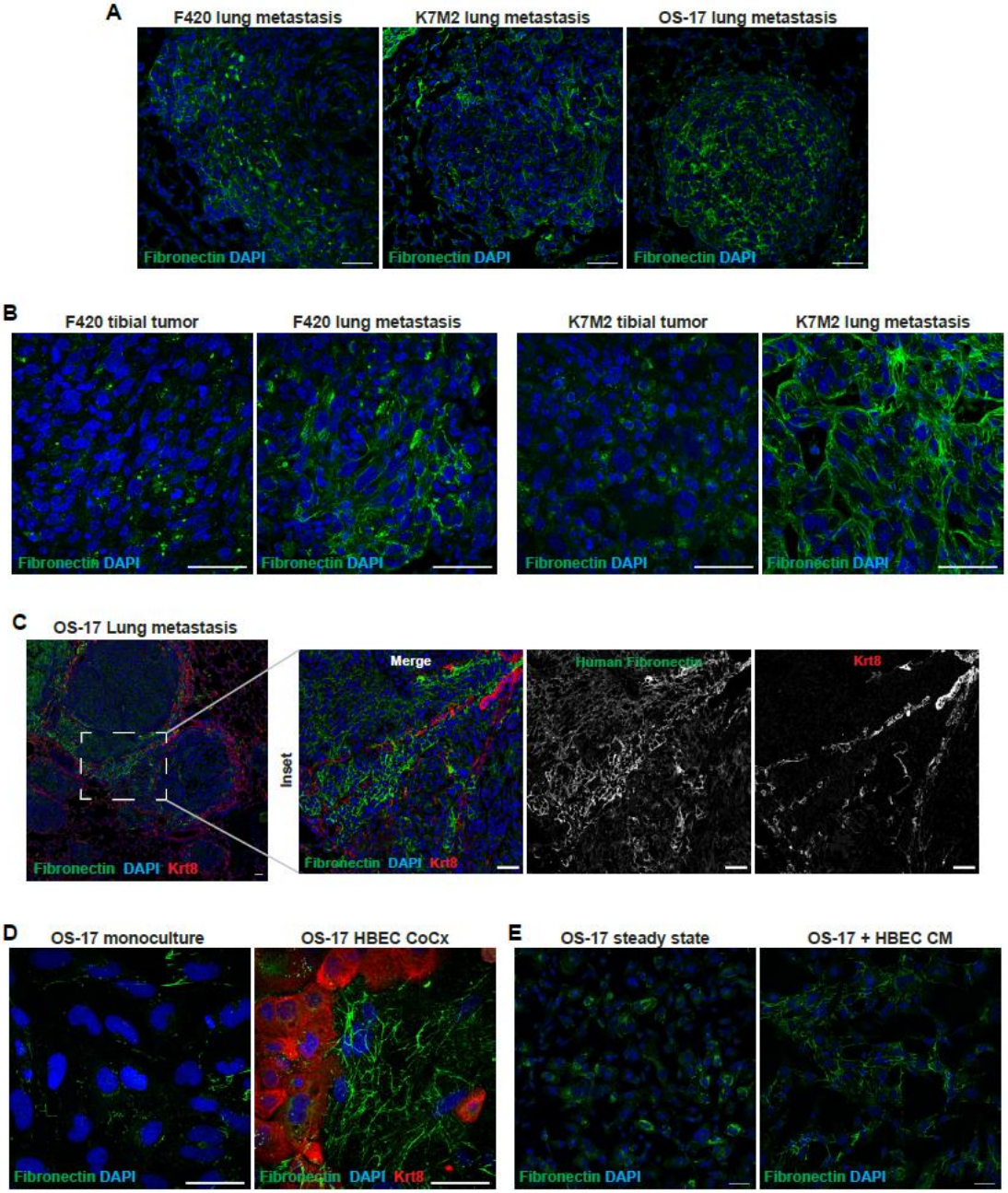

Figure 4

Lung epithelial cells induce metastasis-specific osteosarcoma fibronectin matrix formation. **A,** IHC for fibronectin in several osteosarcoma metastasis models. **B,** IHC comparing fibronectin staining in tibial tumors vs lung metastasis. **C,** IHC for fibronectin (green) and Krt8 (red; DATP cells), dotted box notes inset, which demonstrates area of metastasis enriched in Krt8+ epithelial cells and human (osteosarcoma) fibrillar fibronectin. **D,** Immunofluorescence of fibronectin matrix in OS-17 cells cultured alone or in coculture with human bronchial epithelial cells (HBEC; KRT8=Red). **E;** Immunofluorescence of fibronectin in OS-17 cells cultured at steady state or stimulated with conditioned HBEC media. Scale bar= 50µm. Nuclei are counterstained with DAPI (blue).

Figure 5: Anti-fibrotic tyrosine kinase inhibitor Nintedanib disrupts metastatic progression

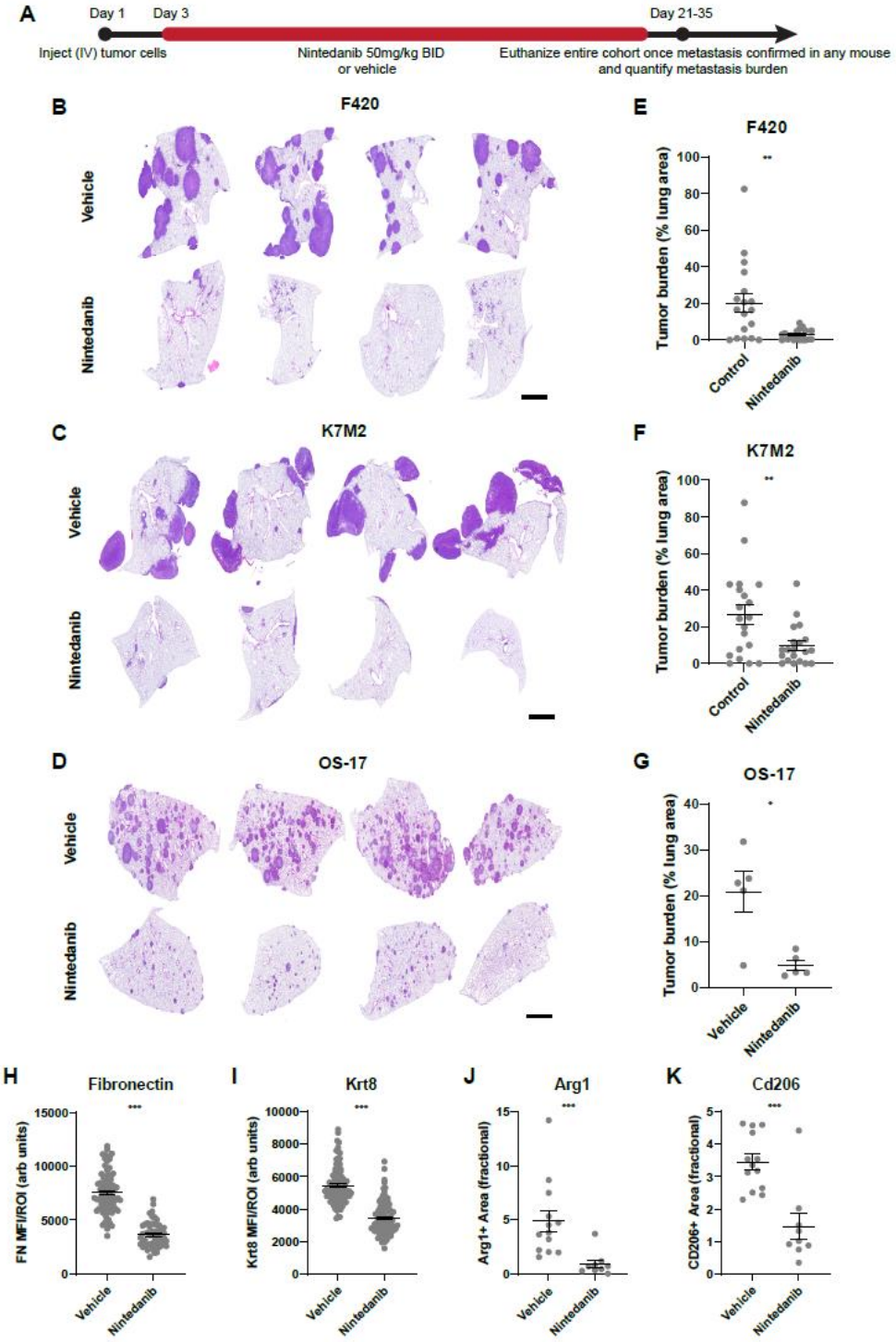

Figure 5

Anti-fibrotic tyrosine kinase inhibitor nintedanib disrupts metastatic progression. **A,** Schematic of nintedanib trial. **B**-**D,** Hematoxylin and eosin staining of representative images from 4 animals from each treatment group. Scale bar= 1000µm. **E-G,** Quantification of tumor burden/lung lobe in vehicle vs nintedanib treated mice. F420 and K7M2 = 20/treatment group, OS-17= 5/treatment group. Welch's t-test F420 p= 0.0030, K7M2 p= 0.0068, OS-17= 0.0199. **H-I,** Quantification of fibronectin (H) and Krt8 (I) in F420 vehicle vs nintedanib treated mice; n=3 animals, at least 10 regions of interest per animal. Welch's t-test p<0.0001. **J-K,** Quantification of chronic wound macrophage by Arg1 (J) and Cd206/Mrc1 in F420 vehicle vs nintedanib treated mice. N=3 animals, at least 10 metastatic lesions/condition quantified as %metastasis area covered by macrophage. Welch's t-test Arg1 p= 0.0017, Cd206 p= 0.0009.